Cryogenic electron spin resonance microimaging probe

Ygal Twig, Ekaterina Dikarov, Aharon Blank *

Schulich Faculty of Chemistry, Technion – Israel Institute of Technology, Haifa 32000, Israel

A R T I C L E   I N F O

A B S T R A C T

A new probe for acquiring ESR images with microscopic resolution and high spin sensitivity, at a temperature range of ~4.2–300 K, is presented. Details of the probe design, as well as its principle of operation, are provided. The probe incorporates a unique surface loop-gap microresonator. Experimental results demonstrate the system's capability to acquire two – as well as three-dimensional images with a flat test sample of phosphorus-doped silicon. The imaging results also allow verifying the resonator's resonance mode – they show its B_1 distribution, which also makes it possible to estimate the number of spins measured in the sample.

© 2012 Elsevier Inc. All rights reserved.

1. Introduction

Electron spin resonance (ESR) is a very useful and robust spectroscopic method with many applications in science and technology [1]. One significant drawback of *conventional* ESR, however, is its relatively low sensitivity compared to other spectroscopic techniques, with commercial systems reaching levels of ~10^9 spins/$\sqrt{Hz}$ at best [2,3]. This sensitivity limitation also affects the available imaging resolution of heterogeneous samples, which in commercial systems reaches ~25 μm [4,5]. This is because, as the image's voxel size decreases, it contains less and less spins and thus quickly runs into the sensitivity limitation "wall". When considering highly specialized home-made systems, a sensitivity of ~10^6 spins/$\sqrt{Hz}$, (or slightly more than 10^4 spins in ~1 h of acquisition) has been recently demonstrated (see also below) [6], and the best pixel resolution achieved in 2D ESR imaging is ~440-nm [7]. In view of the limitations of conventional (known as "induction" or "Faraday") detection techniques, many efforts have been invested in attempts to break these barriers through the use of alternative detection methods. These techniques have attracted considerable interest in the last few years; they have demonstrated resolution improvements from a few microns down to the nanometer scale and have achieved single-electron-spin sensitivity. For example, Scanning Tunneling Microscopy ESR (STM-ESR) [8,9], which combines the high spatial resolution of STM with the electronic spin sensitivity of ESR, can measure the signal from a single spin with ~1-nm 2D resolution. Magnetic Resonance Force Microscopy (MRFM) [10], which detects the force inflicted by the spins on a sharp magnetic tip, shows a single-electron-spin detection capability and 3D nuclear spin imaging with <10-nm resolution [11]. Other methods are not that sensitive yet but have a potential for improvement in the near future. They include, for example, Hall detection [12,13], Superconducting Quantum Interference Device (SQUID) detection [14,15], optically-detected magnetic resonance [16,17], electrically-detected magnetic resonance, [18–20] and indirect detection via diamond nitrogen-vacancy (NV) centers [21–24]. These new methods are very successful and undoubtedly may improve even more in the future. However, as described in details in reference [7], they all have very limited practical use as they require a complex sample preparation measured at extreme physical conditions, and provide surface-only accessibility (a few nanometers deep) and a limited spectroscopic capability. In view of these limitations, it is evident that induction detection may be challenging in terms of sensitivity, but at the end it could prove more rewarding: unlike the unique methods described above, induction detection can be employed in conjunction with all the currently available commercial spectrometers, it does not require special samples or special preparation procedures, and it provides very time-efficient 3D imaging schemes (in contrast to "point-type" imaging schemes, which are mostly limited to the surface or near sub-surface of the new methodologies mentioned above).

In order to examine the prospects and potential paths for improving sensitivity in induction detection we must first take a closer look at the factors affecting it. The signal-to-noise ratio (SNR), which is a measure of the sensitivity of induction–detection pulsed ESR, is given by [25]:

$$SNR_{pulse}^{one\ second} \approx \frac{\sqrt{2\mu_0}M\omega_0 V_V}{8\sqrt{V_c}\sqrt{k_bT(1/\pi T_2^*)}}\sqrt{\frac{Q_u}{\omega_0}}\sqrt{\frac{1}{T_1}}, \qquad (1)$$

* Corresponding author. Fax: +972 4 829 5948.
  E-mail address: ab359@tx.technion.ac.il (A. Blank).

where M is the sample's specific net magnetization (in units of $(JT^{-1} m^{-3})$), as given by the Curie law [26], ω_0 is the Larmor angular frequency, k_b is the Boltzmann constant, T is the temperature, μ_0 is the free-space permeability, and Q_u is the unloaded quality factor of the resonator. The symbol V_c represents the resonator's effective volume [7,25,27,28], which is equal to the volume of a small hypothetical sample V_v (for example, $(1 \, \mu m)^3$), usually located at the point where the resonator's microwave magnetic field is maximal, divided by the filling factor [29] of this small sample [27]. Here we assumed an averaging with a repetition rate equal to $1/T_1$ for SNR improvement and that the bandwidth of excitation is chosen to match the linewidth of the examined paramagnetic species in the sample, $\Delta f = 1/\pi T_2^*$. If T_2 is much larger than T_2^*, additional averaging (with CPMG sequence [30], for example) can increase sensitivity by a factor of $\sim \sqrt{(T_2/2T_2^*)}$.

The relevant controllable parameters in Eq. (1) are: the resonator's volume, V_c, the resonator's quality factor, Q_u, the temperature, T, and the magnetic field (as expressed by the Larmor frequency, ω_0). It should be noted that the magnetic field and the temperature also influence implicitly the sample relaxation times and the net specific magnetization, M, through the Boltzmann population distribution of the spin's energy levels.

Our recent work made use of this parametric dependence in an attempt to minimize the resonator's size, increase its quality factor, and work at lower temperatures and larger static magnetic fields. For example, we built a miniature dielectric resonator with typical dimensions of ~ 1 mm which operates at a relatively high field of $\sim 1.2T$ at room temperature. These characteristics enabled us to attain spin sensitivity of $\sim 1.6 \times 10^8$ spins/$\sqrt{Hz}$ [31]. Furthermore, the small resonator facilitates the use of miniature and highly efficient gradient coils that are placed right around it and can be used to spatially encode the sample, thus obtaining image resolution in the sub-micrometer range [7,31]. More recently, we engaged in the development of a unique type of efficient surface loop-gap microresonators that provide a considerable reduction of the resonator's effective volume (down to a few nanoliters, when operating at Ku band), but which have a rather low quality factor of ~ 15 at room temperature [28]. They have been improved to a smaller design with an effective volume of less than 1 nl [6].

In addition to reducing the resonator's volume it is also possible to turn down the temperature "knob" in the hope of increasing sensitivity, which has a $1/T^{3/2}$ dependence as shown in Eq. (1) (magnetization, M is inversely proportional to temperature). This, however, does not always work to our advantage because in many cases T_1 also increases considerably at low temperatures, limiting the signal acquisition repetition rate. However, if we look at cases where T_1 and T_2 increase in the same manner, one can use multiple echo CPMG pulse sequences to acquire signals in an optimal manner. This is the case in many solid state samples; as noted above, one of our small resonators, which was also incorporated in a cryostat that facilitates measurements in the entire temperature range of ~ 3–300 K, achieved with this method spin sensitivity of $\sim 1.5 \times 10^6$ spins/$\sqrt{Hz}$ for a sample of phosphorus-doped ^{28}Si (denoted $^{28}Si{:}P$) [6].

Here, we will present the details of the cryogenic probe design that enabled the latter measurement. Furthermore, we will show how we integrated into the ESR spectroscopic probe design a set of miniature gradient coils that enable, along with our imaging hardware [31], the obtention of images of samples at a wide range of temperatures. Specific experimental examples of two- and three-dimensional (2D and 3D) images of the $^{28}Si{:}P$ sample used at 10 K in our previous work will be provided. The experiments verify the intense microwave B_1-field focusing of the small surface resonator and its spatial distribution (the "resonance mode"). The potential applications embedded in such high spin sensitivity capability, carried out at a wide range of temperatures and

combined with the possibility of obtaining high-resolution ESR images, range from biology to materials science and physics [27]. For example, ESR micro-/nano-imaging can be used for examining point defects and impurities in semiconductors [32]. This capability is of extreme importance in the development of semiconductor devices, which are characterized by a very small size, and especially in improving the performance of solar cells that is often limited by paramagnetic defects [33,34]. Other potential uses range from the observation of fixed biological samples with stable free radicals [35] up to possibly even addressing issues related to quantum computing [36,37].

2. The cryogenic microimaging probe

Figs. 1–6 present in details the mechanical design of the cryogenic microimaging probe and the resonator used in this work. This structure will be described by reference to its main functions: (a) Delivering a microwave signal in and out of the resonator; (b) Adjusting the coupling of the resonator to the microwave input line; and (c) Delivering gradient drive and piezo control into the probe.

(a) *Microwave signal:* The signal comes into the probe through an SMA connector located on the probe's cap (see Fig. 1a). It then goes down along the center of the probe through a 0.085" stainless steel semi-rigid cable (with low thermal conductivity), until it reaches a connection with a 0.047" non-magnetic copper semi-rigid cable. Reverting now to Fig. 3, it is possible to see how this copper cable is connected to the microstrip line via a brass transition. This microstrip line goes directly under the resonator and excites its resonance mode, as seen also in Fig. 4b and c. The copper semi-rigid cable is held fixed in space by a brass holder (drawn in purple in Figs. 1 and 2). The design in Figs. 3 and 4 features the use of a miniature surface loop-gap resonator made of copper deposited on a rutile substrate. This structure is described in detail (including design method, quality factor and equivalent circuit, and construction method) in our recent works [6,28]. Fig. 4b and c shows two possibilities for the resonator position with respect to the microstrip line, and Fig. 4a presents the dimensions of the resonator used in this work. In this type of resonator, the sample is placed on its surface [6,28]. The imaging probe can also be used with other types of resonators, such as the small (~ 2.4 mm o.d., ~ 1 mm i.d.) cylindrical dielectric resonator used in our room-temperature (RT) microimaging probes [7,31]. In such type of resonator (not drawn here), the sample is placed either inside or above it [31].

(b) *Adjustable coupling:* In principle, there are two main problems facing researchers during the design and operation of ESR probes for low cryogenic temperatures. The first is exchanging samples and the second is achieving variable coupling between the microwave feed and the resonator. In our case, due to the relative complexity of the probe and resonator, we prefer to exchange samples outside the probe, at room temperature, and then insert the probe into the cryostat and gradually lower the temperature. This is a limitation, but since all relevant samples are either solids with an "infinite" life time, or frozen liquids at low temperatures, it is not a major problem. Variable coupling, however, is an important feature that we cannot avoid. This is because, as temperature changes, the properties of the resonator and the feed line also change – causing a significant variation in the coupling properties. In our case the microstrip line is held fixed in space with respect to the probe
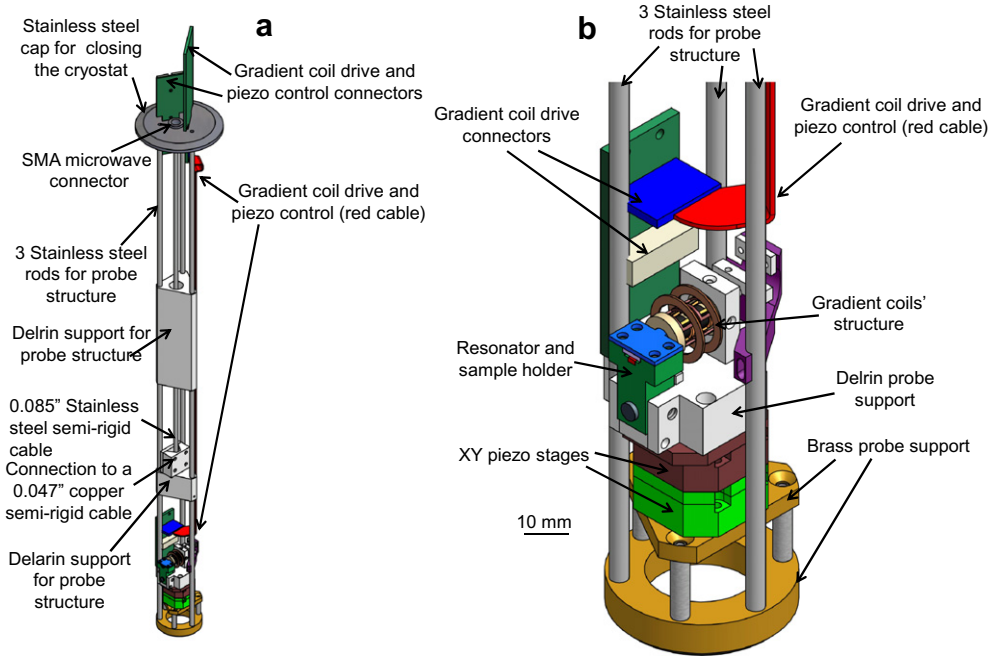
Fig. 1. Schematic drawings of the cryogenic imaging probe. (a) The entire probe, total length of 40 cm (inserted vertically into the cryostat). (b) Close-up view of the lower part of the probe.
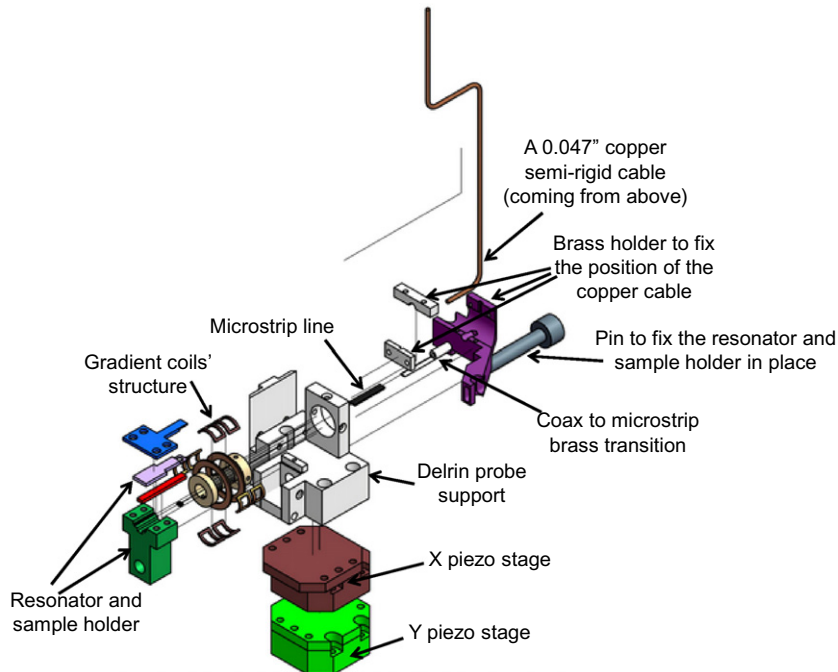

Fig. 2. Enlarged drawing of the lower part of the probe.

support, while the resonator, sample holder, and gradient coil assembly are all connected to the Delrin probe support shown in Figs. 1, 2 and 5, which is mounted on a movable piezoelectric XY stage (model ANP101/RES by AttoCube Systems AG, Germany), as depicted in Figs. 1b and 2. The movement of the stage changes the position of the resonator with respect to the microstrip line (see Fig. 4b and c), which effectively controls the coupling and allows optimizing it at a wide range of temperatures.

(c) *Gradient drive and piezo control:* Fig. 1 shows two electronic circuit boards (painted green[1]) protruding from the top of the probe. The boards are connected to external cables from our gradient drivers [31] and the piezo control from the Atto-cube control box. The signals go from these boards through

---

[1] For interpretation of color in 'Figs. 1–4, 6 and 7', the reader is referred to the web version of this article.
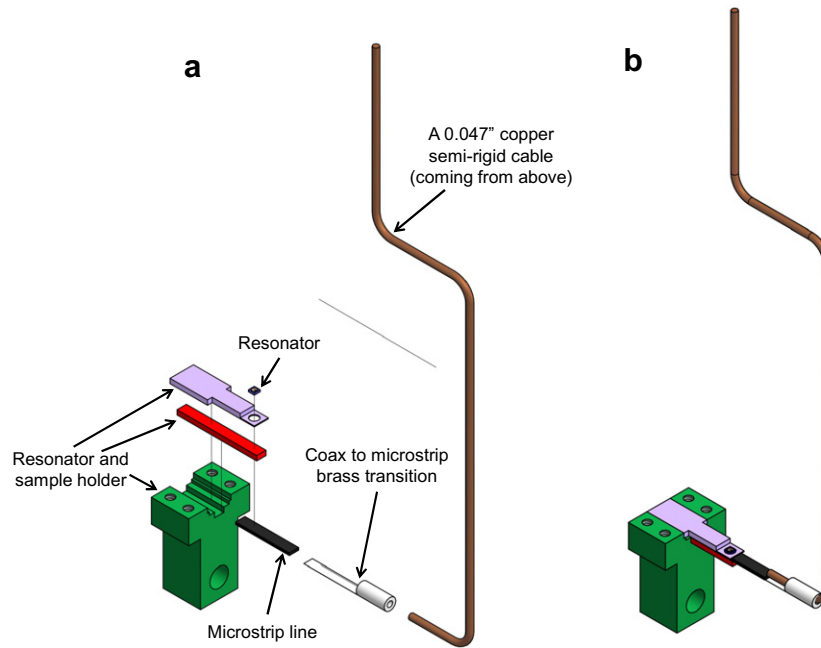
Fig. 3. (a) Enlarged drawing providing details of the resonator and sample holder. (b) The resonator and sample holder assembly.
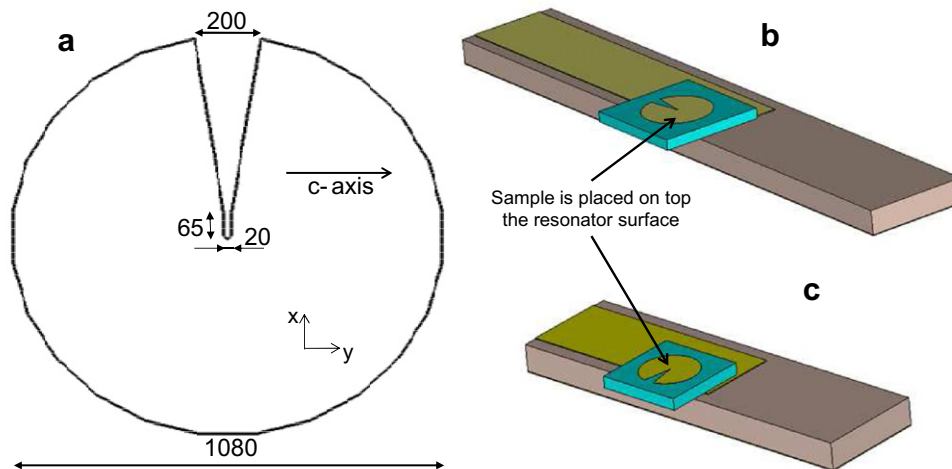

Fig. 4. (a) The dimensions (in μm) on the resonator used in this work. (b and c) Two optional resonator excitation schemes.

the red cable and into another circuit board in the lower part of the probe (see Fig. 1b), from which they later continue toward the gradient coils and the piezo stages.

The array of gradient coils used here (Fig. 6) is similar to the one we used in the RT works but with slight modifications [7,25,31,38–40]. Refs. [7,25,31,38–40] also contain detailed information about the gradient coils' specifications, dimensions, properties and construction procedure. The coils are placed on a thin (4.4-mm i.d, 4.6-mm o.d) rexolite tube covered with a 1-μm gold layer. The gold shields the resonator at microwave frequencies, but it is transparent to the pulsed magnetic field gradients whose spectral range reaches a maximum of only ∼10 MHz (for 100-ns pulses). This shielding makes it possible to maintain a relatively high quality (Q) factor (typically ∼1000) for the dielectric resonators, but is less important for the surface resonators that have a smaller Q and

smaller relative radiation losses to begin with. The X-, Y-, and Z-gradient coils are arranged around the cylindrical shield together with the regular DC bias coils (see Fig. 6). The structure and properties of these coils are identical to the ones in the ∼17-GHz RT imaging probe described in [7]. The maximum magnetic field gradient achieved by this system (for the X and Y coils) with short (0.5–1 μs) current pulses of 95 A (coming out of an 1100-V source [31,41]) is ∼130 T/m with a repetition rate of ∼20–40 kHz. One of the major problems in generating such strong gradients at such a high-repetition rate is the excessive heat generated by the coils. In order to prevent this problem, the coils are embedded in a heat-conducting (but electrical insulator) adhesive (Arctic Alumina™ with heat conductivity >4 W/mK by Arctic Silver Inc., USA). Furthermore, the continuous flow of cold helium vapor in the cryostat efficiently dissipates the heat generated in the coil. The imaging probe can accommodate flat samples (when used
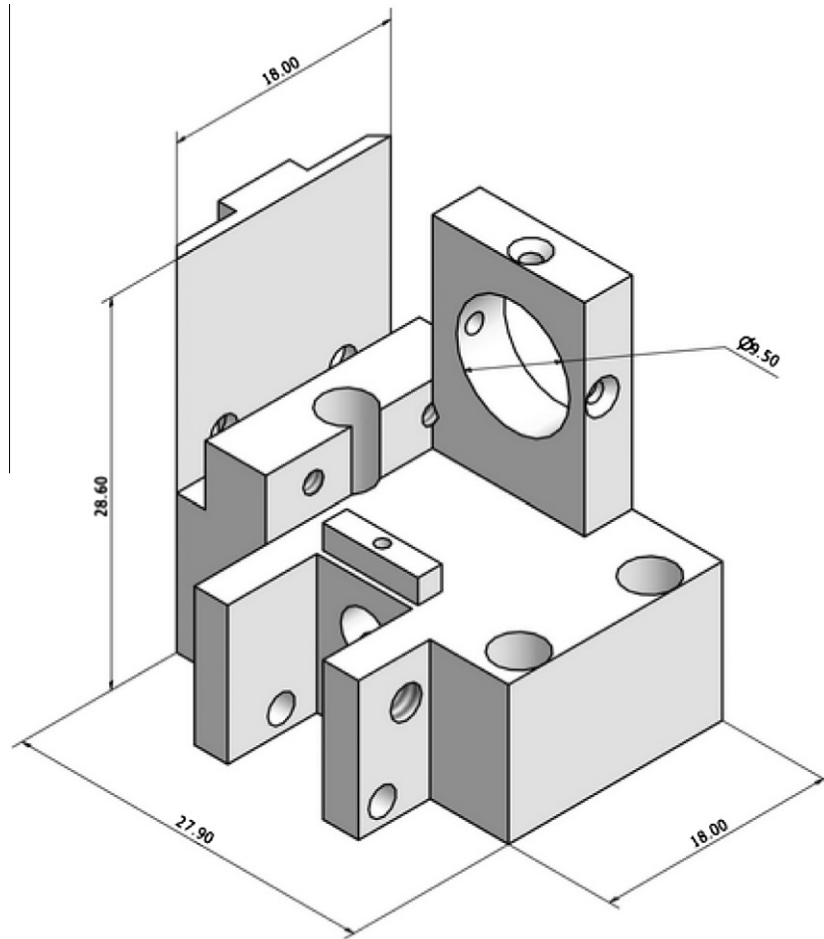
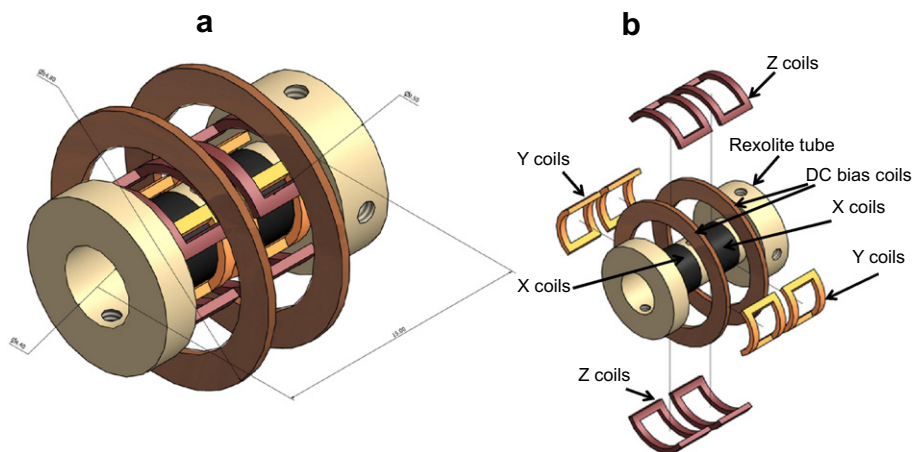**Fig. 5.** Drawing of the main Delrin probe support.

Fig. 6. (a) The gradient coil structure. (b) Enlarged drawing of the gradient coil structure. X coils are in black – Maxwell pair; Y coils are shown in yellow – Golay gradient coils; Z coils are in brown, also Golay geometry; and a regular Helmholtz pair above all coils, to lock the static field on the resonance line (field frequency lock).

with a surface resonator) or cylindrical samples with a diameter of $\sim$1 mm and a height of $\sim$0.5–1 mm (when a dielectric resonator is used).

Our imaging system hardware and software can support a wide variety of pulsed imaging acquisition modes, as detailed in Ref. [31]. In this work we added the possibility of using a CPMG imaging sequence, as described in Fig. 7. Such sequence is useful when T_2^* is much shorter than T_2. In such a case, many echoes can be

acquired and averaged together in the CPMG sequence without significant decay, leading to an increased SNR.

3. Experimental results and discussion

The aim of the experiments presented here is to verify the proper operation of the imaging probe at low temperatures (the
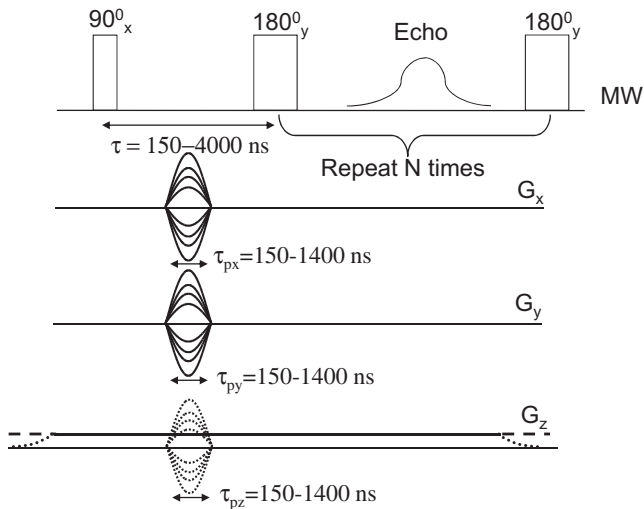
Fig. 7. Imaging pulse sequences that the system can support.

room-temperature operation of a similar gradient coil setup was already shown in [7,31]). The test sample used is the same one employed in our recent study [6], made of a 10-μm layer of phosphorous-doped ^{28}Si (termed ^{28}Si:P) with a concentration of 10^{16} P atoms per cm^3, on top of a 500-μm-thick intrinsic Si wafer. The sample was cut from a Si wafer originally manufactured by the ISONICS Corporation, USA, which also characterized it in terms of doping concentration (by Hall bar measurements) and doping layer thickness (see also [42]). We did not carry out an independent characterization of this sample, except for measuring its ESR linewidth, which was found to be less than 0.1 G. This is a clear indication that the doping concentration is below $\sim 2 \times 10^{16}$ P atoms per cm^3 since higher concentrations cause significant line broadening [43,44]. This test sample is homogeneous and flat, and thus suitable for the surface resonator employed here. The spatially-resolved information imaged is therefore not the geometry of the spin concentration in the sample but rather the microwave mode of the resonator. Fig. 8c shows the results of a typical two-dimensional ESR imaging experiment for this type of sample, measured at a temperature of 10 K. The imaging sequence employed here is described in Fig. 7 (CPMG), using only G_x and G_y. For the ^{28}Si:P sample such sequence is more favorable than a simple Hahn echo imaging

sequence (see for example [31]). This is because T_2^* (~ 0.8 μs at 10 K) is much shorter than T_2 (~ 260 μs), and thus multiple echoes can be refocused for a single 90° pulse, leading to a significant increase in the SNR. The specific pulse sequence parameters are: $\tau = 2000$ ns, $N = 100$, and the repetition rate was 1000 Hz, to be compatible with the T_1 of this sample at 10 K (~ 1 ms). The values of τ_{px} and τ_{px} are ~ 600 and 700 ns, respectively, with peak gradient values of ~ 52 T/m, and the microwave frequency used is 12.4 GHz. The acquisition time for the ESR image is 102 min. The total image size is 160×120 pixels and the pixel size is $\sim 1.8 \times 1.5$ μm.

The imaging results are compared to the square of the calculated magnetic field component, B_1^2, of the resonator's microwave mode (close-up view of the resonance mode in Fig. 2 of Ref. [6]). This quantity is roughly proportional to the ESR signal magnitude (although the exact dependence on the B_1 magnitude for such pulsed experiment is somewhat more complex, see the discussion in Ref. [28]). The comparison to the calculations is made for two surfaces, one located at a height of 1 μm above the resonator's surface and the second at a height of 5 μm. Since the B_1^2 of this resonator drops by a factor of ~ 4 for such a short distance [6], it is expected that the 2D signal, which is the projected integral sum of the entire 10-μm-thick sample, will be heavily weighted towards the field distribution at shorter distances from the surface. Indeed, Fig. 8c resembles a cross between Fig. 8a and b with some distortions that may be caused by production problems in the lithography process, a non-clean resonator surface, and misalignments between the gradient axes and those of the resonator (leading to the image being tilted). Based on the image's pixel size (see above) and the known sample concentration, it is possible to estimate that there are $\sim 270,000$ spins in each $\sim 1.8 \times 1.5 \times 10$-μm voxel. In practice, however, due to the sharp decrease in the microwave B_1 going out of the plane of the resonator (see calculation in Fig. 2 of Ref. [6]), most of the signal is obtained from a much smaller volume extending not more than ~ 3–5 μm above the resonator. This provides an estimated number of $\sim 10^5$ "effective" spins per voxel as a good representative figure. The sharp exponential decrease in B_1 going out of plane was not verified by imaging, due to lack of sufficient resolution and a slight misalignment of the axis of the Z-gradient with respect to the sample normal – see below.

The noise in the image can be divided into two types: random noises that can be found in voxels far away from the peak signals in the image, and artifact noises that can appear as "shadows" or "mirrors" of the main signal. The random noise in the image is
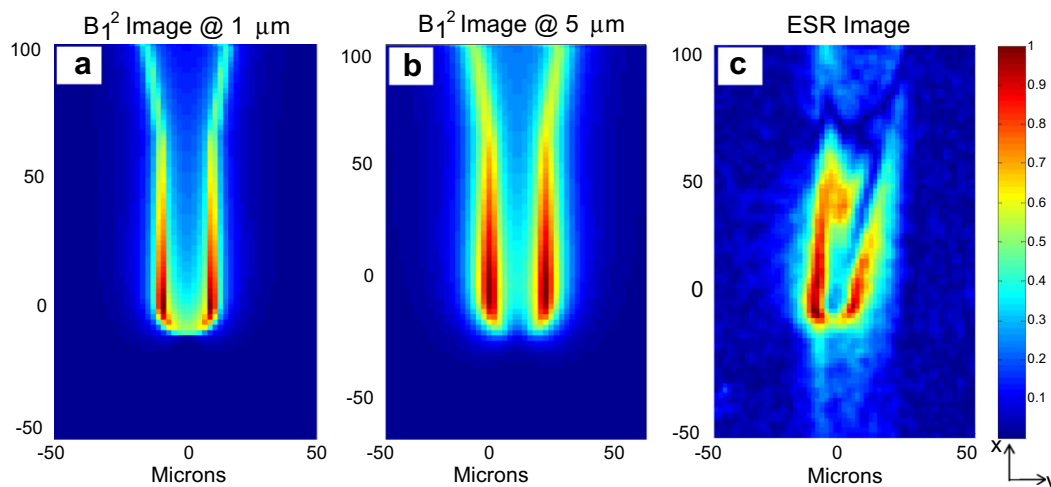

Fig. 8. Results of the two-dimensional ESR imaging vs. the calculated B_1^2 of the resonator. (a) The calculated fields at a height of 1 μm above the metallic plane of the resonator. (b) The calculated fields at a height of 5 μm above the metallic plane of the resonator. Two-dimensional ESR image of a flat ^{28}Si:P sample placed on the resonator.
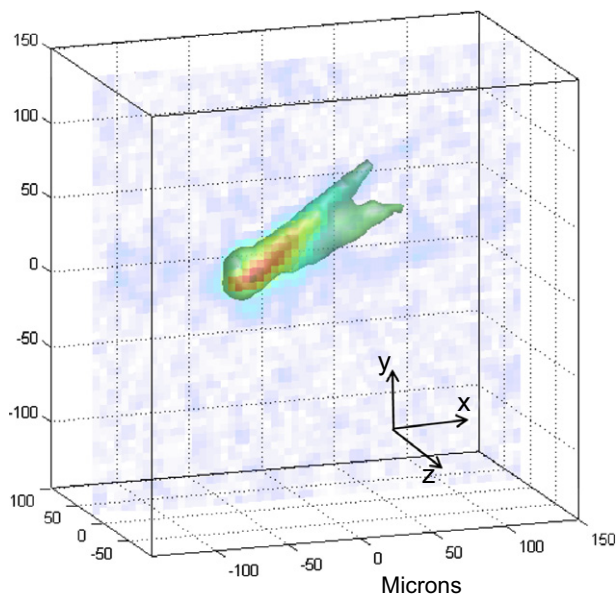
Fig. 9. Volume plot of a three-dimensional ESR image of the same sample as in Fig. 8. A 2D cut along the sample's z axis is superimposed on the volume plot.

rather low, with an estimated peak signal vs. RMS noise of ∼25. This results in an absolute spin sensitivity of ∼10^5/25 = 4000 spins for the measurement time employed here, or ∼114 net spins (considering the Boltzmann factor of ∼35 at 10 K and 12.4 GHz). I.e., a quantity of ∼4000 spins of the ^{28}Si:P sample, placed in a voxel located in the most sensitive region of the resonator, would provide, after ∼2 h averaging time, an SNR of 1. The artifact noise is visible mainly along the x axis of the image (notice that the image axes were rotated by 90° in Fig. 8) and it is caused by k-space coverage method (fast along the x axis and slow along the y axis). Some "blurring" of the image may also be attributed to the long acquisition time, during which some drifts may occur. Also, the relatively long T_2 of the sample can lead to some blurring due to phase noise from the electromagnet [45]. Finally, an important point that should be made is that, for a large B_1 inhomogeneity, the even echoes in the CPMG sequence have a different phase than the odd echoes. This issue was discussed in details in Refs. [46–48], along with methods for eliminating this artifact. Here we simply summed up all the echoes, which resulted in two identical images that are mirrored to each other. If the images are far enough from the symmetry plane (as was the case here) it is possible to simply add them up after inverting one of them.

Fig. 9 shows the results of three-dimensional imaging using the same sample and resonator, also measured at 10 K. Here we employed the imaging sequence shown in Fig. 7 with full phase encoding in all three axes. For the x and y axes, gradient pulses similar to the ones employed in the 2D experiments were used, but with a peak gradient of ∼15 T/m. For the z axis, the gradient pulse had a τ_{pz} of ∼500 ns and a peak gradient of ∼20 T/m. The total image size is 120 × 120 × 80 voxels and the image's pixel size is ∼6.2 × 5.2 × 5.7 μm. The image acquisition time is 10 h and the SNR is ∼31. The image shows a 3D volume plot superimposed on a 2D cut along the z axis. The cut shows that the plane of the z axis gradients is not exactly parallel to the plane of the flat sample (it goes through the sample in a somewhat slanted manner).

4. Conclusions

A new probe which enables the acquisition of microscopic ESR images with high spin sensitivity and high spatial resolution, at temperatures ranging from ∼4.2 to 300 K, was presented. At low temperatures with a test sample of ^{28}Si:P, the estimated spin sensitivity is ∼4000 spins with an acquisition time of less than 2 h, provided they are placed in the most sensitive region of the resonator. This is an exceptionally optimal sample, given that its T_1 and T_2 properties allow for efficient averaging at a high-repetition rate. Other types of samples (Trityl solution, N@C$_{60}$) show lower sensitivity – see Ref. [6]; in general, the dependence of spin sensitivity and image resolution upon sample properties was described in detail in Refs. [25,40]. The high resolution ESR images we obtained make it possible to verify the resonance mode of our unique surface resonator and also to estimate the actual number of measured spins in our sample. The cryogenic probe can be useful for a variety of applications requiring high spin sensitivity and high spatial resolution in samples such as thin-film solar cells [33], measurements of paramagnetic monolayers [49] and, in general, for measuring spin-limited samples.

References

[1] S.K. Misra, Multifrequency Electron Paramagnetic Resonance, Theory and Applications, Wiley-VCH, Berlin, 2011.
[2] D. Schmalbein, G.G. Maresch, A. Kamlowski, P. Hofer, The Bruker high-frequency-EPR system, Appl. Magn. Reson. 16 (1999) 185–205.
[3] Bruker, <http://www.bruker-biospin.com/cwperformance-sense.html>, 2012.
[4] Bruker, <http://www.bruker-biospin.com/eprimaging0.html>, 2012.
[5] Bruker, EPR News Letter, EPR News Letter 2010 (2010) p. 18.
[6] Y. Twig, E. Dikarov, W.D. Hutchison, A. Blank, Note: high sensitivity pulsed electron spin resonance spectroscopy with induction detection, Rev. Sci. Instrum. 82 (2011) 076105.
[7] A. Blank, E. Suhovoy, R. Halevy, L. Shtirberg, W. Harneit, ESR imaging in solid phase down to sub-micron resolution: methodology and applications, Phys. Chem. Chem. Phys. 11 (2009) 6689–6699.
[8] Y. Manassen, R.J. Hamers, J.E. Demuth, A.J. Castellano, Direct observation of the precession of individual paramagnetic spins on oxidized silicon surfaces, Phys. Rev. Lett. 62 (1989) 2531–2534.
[9] C. Durkan, M.E. Welland, Electronic spin detection in molecules using scanning-tunneling-microscopy-assisted electron-spin resonance, Appl. Phys. Lett. 80 (2002) 458–460.
[10] D. Rugar, R. Budakian, H.J. Mamin, B.W. Chui, Single spin detection by magnetic resonance force microscopy, Nature 430 (2004) 329–332.
[11] C.L. Degen, M. Poggio, H.J. Mamin, C.T. Rettner, D. Rugar, Nanoscale magnetic resonance imaging, Proc. Natl. Acad. Sci. USA 106 (2009) 1313–1317.
[12] G. Boero, P.A. Besse, R. Popovic, Hall detection of magnetic resonance, Appl. Phys. Lett. 79 (2001) 1498–1500.
[13] P. Kejik, G. Boero, M. Demierre, R.S. Popovic, An integrated micro-hall probe for scanning magnetic microscopy, Sens. Actuat. A-Phys. 129 (2006) 212–215.
[14] R. McDermott, A.H. Trabesinger, M. Muck, E.L. Hahn, A. Pines, J. Clarke, Liquid-state NMR and scalar couplings in microtesla magnetic fields, Science 295 (2002) 2247–2249.
[15] C.I. Pakes, P.W. Josephs-Franks, R.P. Reed, S.G. Corner, M.S. Colclough, Development of miniature DC SQUID devices for the detection of single atomic spin-flips, IEEE Trans. Instrum. Meas. 50 (2001) 310–313.
[16] J. Wrachtrup, C. Vonborczyskowski, J. Bernard, M. Orrit, R. Brown, Optical-detection of magnetic-resonance in a single molecule, Nature 363 (1993) 244–245.
[17] J. Kohler, J.A.J.M. Disselhorst, M.C.J.M. Donckers, E.J.J. Groenen, J. Schmidt, W.E. Moerner, Magnetic-resonance of a single molecular spin, Nature 363 (1993) 242–244.
[18] W. Harneit, C. Boehme, S. Schaefer, K. Huebener, K. Fostiropoulos, K. Lips, Room temperature electrical detection of spin coherence in C$_{60}$, Phys. Rev. Lett. 98 (2007) 216601.
[19] D.R. McCamey, H. Huebl, M.S. Brandt, W.D. Hutchison, J.C. McCallum, R.G. Clark, A.R. Hamilton, Electrically detected magnetic resonance in ion-implanted Si:P nanostructures, Appl. Phys. Lett. 89 (2006).
[20] A.R. Stegner, C. Boehme, H. Huebl, M. Stutzmann, K. Lips, M.S. Brandt, Electrical detection of coherent P-31 spin quantum states, Nat. Phys. 2 (2006) 835–838.

[21] G. Balasubramanian, I.Y. Chan, R. Kolesov, M. Al-Hmoud, J. Tisler, C. Shin, C. Kim, A. Wojcik, P.R. Hemmer, A. Krueger, T. Hanke, A. Leitenstorfer, R. Bratschitsch, F. Jelezko, J. Wrachtrup, Nanoscale imaging magnetometry with diamond spins under ambient conditions, Nature 455 (2008) 648–651.

[22] J.R. Maze, P.L. Stanwix, J.S. Hodges, S. Hong, J.M. Taylor, P. Cappellaro, L. Jiang, M.V.G. Dutt, E. Togan, A.S. Zibrov, A. Yacoby, R.L. Walsworth, M.D. Lukin, Nanoscale magnetic sensing with an individual electronic spin in diamond, Nature 455 (2008) 644–647.

[23] J.M. Taylor, P. Cappellaro, L. Childress, L. Jiang, D. Budker, P.R. Hemmer, A. Yacoby, R. Walsworth, M.D. Lukin, High-sensitivity diamond magnetometer with nanoscale resolution, Nat. Phys. 4 (2008) 810–816.

[24] P. Hemmer, B. Grotz, J. Beck, P. Neumann, B. Naydenov, R. Reuter, F. Reinhard, F. Jelezko, J. Wrachtrup, D. Schweinfurth, B. Sarkar, Sensing external spins with nitrogen-vacancy diamond, New J. Phys. 13 (2011) 055004.

[25] A. Blank, J.H. Freed, ESR microscopy and nanoscopy with "induction" detection, Isr. J. Chem. 46 (2006) 423–438.

[26] G.A. Rinard, R.W. Quine, R.T. Song, G.R. Eaton, S.S. Eaton, Absolute EPR spin echo and noise intensities, J. Magn. Reson. 140 (1999) 69–83.

[27] A. Blank, C.R. Dunnam, P.P. Borbat, J.H. Freed, High resolution electron spin resonance microscopy, J. Magn. Reson. 165 (2003) 116–127.

[28] Y. Twig, E. Suhovoy, A. Blank, Sensitive surface loop-gap microresonators for electron spin resonance, Rev. Sci. Instrum. 81 (2010) 104703.

[29] C.P. Poole, Electron Spin Resonance: A Comprehensive Treatise on Experimental Techniques, 2nd ed., Wiley, New York, 1983.

[30] S. Meiboom, D. Gill, Modified spin-echo method for measuring nuclear relaxation times, Rev. Sci. Instrum. 29 (1958) 688–691.

[31] L. Shtirberg, Y. Twig, E. Dikarov, R. Halevy, M. Levit, A. Blank, High-sensitivity Q-band electron spin resonance imaging system with submicron resolution, Rev. Sci. Instrum. 82 (2011) 043708.

[32] M. Kondo, S. Yamasaki, A. Matsuda, Microscopic structure of defects in microcrystalline silicon, J. Non-Cryst. Solids 266 (2000) 544–547.

[33] M. Weizman, L.P. Scheller, N.H. Nickel, K. Lips, B. Yan, Electron spin resonance in laser-crystallized polycrystalline silicon-germanium thin films, Phys. Stat. Solid. A-Appl. Mater. Sci. 207 (2010) 570–573.

[34] B. Rech, T. Roschek, T. Repmann, J. Muller, R. Schmitz, W. Appenzeller, Microcrystalline silicon for large area thin film solar cells, Thin Solid Films 427 (2003) 157–165.

[35] M. Savla, R.P. Pandian, P. Kuppusamy, G. Agarwal, Magnetic force microscopy of an oxygen-sensing spin-probe, Isr. J. Chem. 48 (2008) 33–38.

[36] W. Harneit, C. Meyer, A. Weidinger, D. Suter, J. Twamley, Architectures for a spin quantum computer based on endohedral fullerenes, Phys. Stat. Solid B-Basic Res. 233 (2002) 453–461.

[37] B.E. Kane, A silicon-based nuclear spin quantum computer, Nature 393 (1998) 133–137.

[38] A. Blank, C.R. Dunnam, P.P. Borbat, J.H. Freed, 3D Continuous wave electron spin resonance microscope, Rev. Sci. Instrum. 75 (2004) 3050–3061.

[39] A. Blank, R. Halevy, M. Shklyar, L. Shtirberg, P. Kuppusamy, ESR micro-imaging of LiNc–BuO crystals in PDMS: spatial and spectral grain distribution, J. Magn. Reson. 203 (2010) 150–155.

[40] A. Blank, Multifrequency Electron Paramagnetic Resonance, Theory and Applications, Wiley-VCH, Berlin, 2011 (Chapter 19).

[41] L. Shtirberg, A. Blank, Short, powerful, and agile current drivers for magnetic resonance, Concepts Magn. Reson. Part B: Magn. Reson. Eng. 39B (2011) 119–127.

[42] L. Alexander, K.N. Suwuntanasarn, W.D. Hutchison, Phosphorus spin coherence times in silicon at very low temperatures, Cond.-Mat.Mtrl.-Sci. arXiv:1009.4240v1 (2010).

[43] P.R. Cullis, J.R. Marko, Electron-paramagnetic resonance properties of N-type silicon in intermediate impurity-concentration range, Phys. Rev. B 11 (1975) 4184–4200.

[44] G. Feher, E.A. Gere, Electron spin resonance experiments on donors in silicon II electron spin relaxation effects, Phys. Rev. 114 (1959) 1245–1256.

[45] A.M. Tyryshkin, S.A. Lyon, A.V. Astashkin, A.M. Raitsimring, Electron spin relaxation times of phosphorus donors in silicon, Phys. Rev. B 68 (2003).

[46] A. Blank, S. Ish-Shalom, L. Shtirberg, Y. Zur, Ex situ endorectal MRI probe for prostate imaging, Magn. Reson. Med. 62 (2009) 1585–1596.

[47] Y. Zur, An algorithm to calculate the NMR signal of a multi spin-echo sequence with relaxation and spin-diffusion, J. Magn. Reson. 171 (2004) 97–106.

[48] Y. Zur, S. Stokar, A phase-cycling technique for canceling spurious echoes in NMR imaging, J. Magn. Reson. 71 (1987) 212–228.

[49] M. Mannini, D. Rovai, L. Sorace, A. Perl, B.J. Ravoo, D.N. Reinhoudt, A. Caneschi, Patterned monolayers of nitronyl nitroxide radicals, Inorg. Chim. Acta 361 (2008) 3525–3528.